AGU ADVANCING EARTH AND SPACE SCIENCES

Geophysical Research Letters

RESEARCH LETTER
10.1029/2024GL109996

Inclusion of Nonresonant Effects Into Quasi-Linear Diffusion Rates for Electron Scattering by Electromagnetic Ion Cyclotron Waves

Xiaofei Shi[1], Xin An[1], Anton Artemyev[1], Xiao-Jia Zhang[1,2], Didier Mourenas[3,4], and Vassilis Angelopoulos[1]

[1]Department of Earth, Planetary, and Space Sciences, University of California, Los Angeles, CA, USA, [2]Department of Physics, University of Texas at Dallas, Richardson, TX, USA, [3]CEA, DAM, DIF, Arpajon, France, [4]Laboratoire Matière en Conditions Extrêmes, Université Paris-Saclay, CEA, Bruyères-le-Châtel, France

Key Points:

- We provide a statistical model of nonresonant electron scattering by electromagnetic ion cyclotron waves
- We show the main wave and electron parametric regions where nonresonant effects can be important for electron precipitation
- We derive an analytical approximation allowing generalization of the quasi-linear diffusion rates including nonresonant effects

Supporting Information:

Supporting Information may be found in the online version of this article.

Correspondence to:

X. Shi,
sxf1698@g.ucla.edu

Citation:

Shi, X., An, X., Artemyev, A., Zhang, X.-J., Mourenas, D., & Angelopoulos, V. (2024). Inclusion of nonresonant effects into quasi-linear diffusion rates for electron scattering by electromagnetic ion cyclotron waves. *Geophysical Research Letters*, *51*, e2024GL109996. https://doi.org/10.1029/2024GL109996

Received 25 APR 2024
Accepted 21 JUN 2024

Abstract Electromagnetic ion cyclotron (EMIC) waves are a key plasma mode affecting radiation belt dynamics. These waves are important for relativistic electron losses through scattering and precipitation into Earth's ionosphere. Although theoretical models of such resonant scattering predict a low-energy cut-off of ∼1 MeV for precipitating electrons, observations from low-altitude spacecraft often show simultaneous relativistic and sub-relativistic electron precipitation associated with EMIC waves. Recently, nonresonant electron scattering by EMIC waves has been proposed as a possible solution to the above discrepancy. We employ this model and a large database of EMIC waves to develop a universal treatment of electron interactions with EMIC waves, including nonresonant effects. We use the Green's function approach to generalize EMIC diffusion rates foregoing the need to modify existing codes or recompute empirical wave databases. Comparison with observations from the electron losses and fields investigation mission demonstrates the efficacy of the proposed method for explaining sub-relativistic electron losses by EMIC waves.

Plain Language Summary Precipitation of energetic electrons from the equatorial magnetosphere to the Earth's ionosphere plays a crucial role in the dynamics of the radiation belt and ionosphere ionization. Such precipitation is primarily driven by wave-particle interactions. However, accurately modeling these interactions requires precise knowledge of the electron energy ranges which is affected by different wave modes present in the equatorial magnetosphere. A notable challenge arises from the contradiction between model-predicted energy ranges of electron precipitation by electromagnetic ion cyclotron (EMIC) waves and the energies observed by spacecraft during such precipitation events. By combining a new theoretical approach with detailed observational data sets of these waves, we successfully resolved this contradiction, offering a powerful tool for the simulation of electron precipitation driven by EMIC waves.

1. Introduction

Electromagnetic ion cyclotron (EMIC) waves play a critical role in controlling the dynamics of relativistic electron fluxes through the resonant scattering of these electrons into the Earth's ionosphere (Millan & Thorne, 2007; Shprits et al., 2008; Usanova, 2021; Yahnin et al., 2017). For realistic plasma and magnetic field conditions in the inner magnetosphere, where EMIC waves are generated (Jun et al., 2019, 2021; Usanova et al., 2012; Zhang et al., 2016), these waves are thought to provide much of the scattering and precipitation of multi-MeV electrons (e.g., Kersten et al., 2014; Ni et al., 2015; Summers & Thorne, 2003; Summers et al., 2007b). However, low-altitude observations of sub-MeV electron precipitation, in conjunction with near-equatorial EMIC waves, demonstrate a discrepancy with theoretical predictions regarding the typical resonance energy range of the main population of intense EMIC waves (An et al., 2022; Capannolo et al., 2019; Hendry et al., 2017, 2019; Yahnin et al., 2016).

Recently, this discrepancy between theory and observations was further underscored by analyses using over 3 yrs of data from the Electron losses and fields investigation (ELFIN) mission, a pair of low-altitude Cubesats (Angelopoulos et al., 2020) measuring precipitating and locally trapped fluxes associated with EMIC wave-driven precipitation events (Angelopoulos et al., 2023; Capannolo et al., 2023). A distinct feature of EMIC wave-driven precipitation, clearly observed at low altitudes, is the presence of a low-energy cutoff in the efficiency of precipitation. This feature, most evident as a low-energy cutoff in the energy spectrum of the

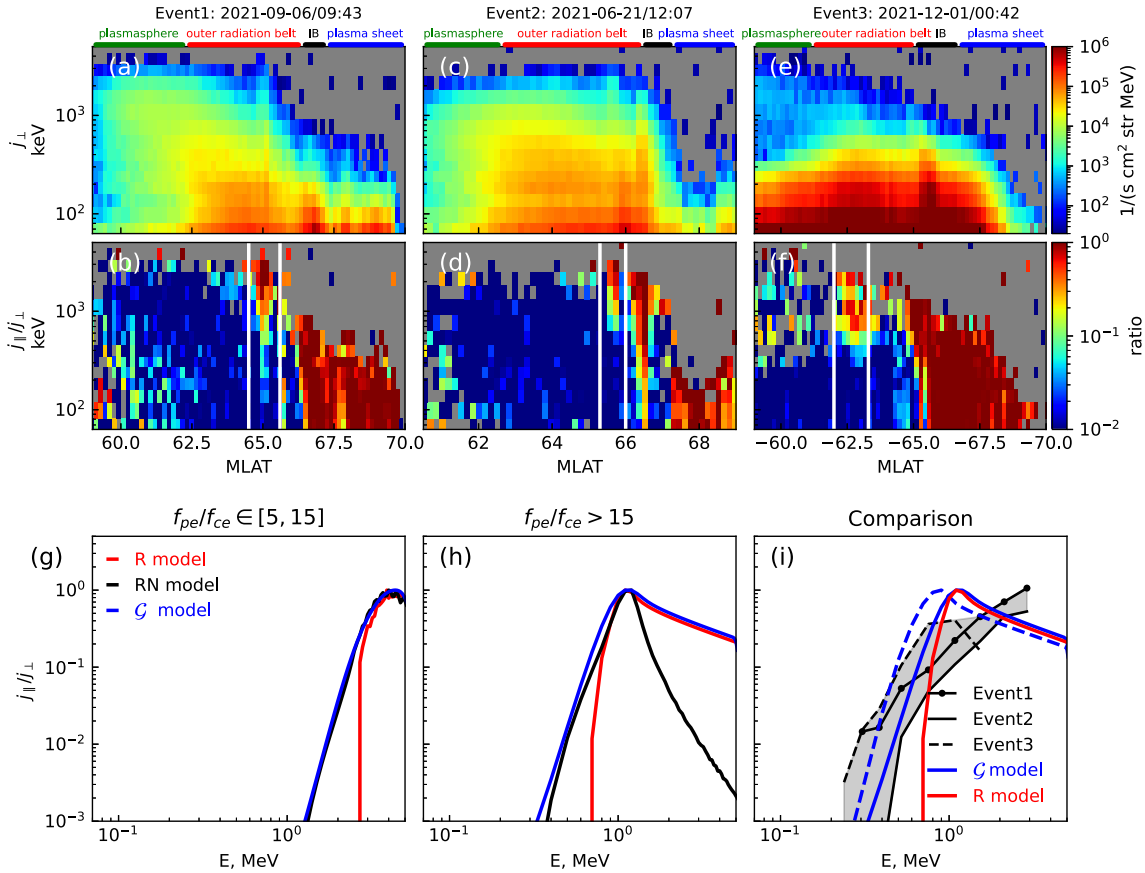

Figure 1. Three examples of electron losses and fields investigation observations of electron precipitation driven by electromagnetic ion cyclotron waves. Panels (a, c, e) and (b, d, f) show spectra of locally trapped (outside the bounce loss-cone) electron fluxes and precipitating-to-trapped flux ratio, $j_\parallel/j_\perp$, respectively. Panel (i) shows the spectra of the precipitating-to-trapped flux ratio (the "precipitation ratio") from intervals between the white lines in panels (b, d, f). Top bars indicate the main regions crossed by ELFIN: the plasma sheet is characterized by <200 keV, isotropic fluxes (precipitation ratio ∼1) (see Artemyev et al., 2022); the isotropy boundary (IB), signifying the transition between plasma sheet and inner magnetosphere, has a clear MLAT-versus-energy dispersion in the precipitation ratio (see Wilkins et al., 2023); the outer radiation belt is characterized by relativistic electrons having high trapped fluxes and low precipitation ratios, except for instances of high precipitation ratios signifying EMIC-driven precipitation (see Angelopoulos et al., 2023); the plasmasphere is characterized by significant fluxes of trapped relativistic electrons and low fluxes of trapped $\lesssim$300 keV electrons, because the latter are scattered quite efficiently by whistler-mode hiss waves and form strongly anisotropic distributions with low fluxes around the loss-cone (see discussion in Ma et al. (2016), Mourenas et al. (2017)). The EMIC-driven electron precipitation events are within the outer radiation belt (between the two white lines), near the expected location of the plasmapause estimated from O'Brien and Moldwin (2003) model. Panels (g, h) compare theoretical results for $j_\parallel/j_\perp$ calculated from the diffusion coefficient obtained with resonant-only interactions (R model) and with the combination of resonant and nonresonant interactions (RN model) for two data sets of different plasma frequency-to-gyrofrequency ratio, $f_{pe}/f_{ce} = 10$ and $f_{pe}/f_{ce} = 20$. Blue curves show the Green's function model ($\mathcal{G}$ model) that fits the RN model. Panel (i) compares the R model (red) and $\mathcal{G}$ model (solid blue for $f_{pe}/f_{ce} = 20$ and dashed blue for $f_{pe}/f_{ce} = 25$) with $j_\parallel/j_\perp$ derived from three events shown in top panels.

precipitating-to-trapped flux ratio (the "precipitation ratio"), indicates the existence of a minimum resonance energy for electron scattering process by EMIC waves. In contrast, alternate scattering mechanisms of relativistic electrons, principally those by whistler-mode waves and magnetic field line curvature, are not expected to exhibit a similar low energy cutoff in the range between 50 and 1,000 keV. To clarify, we note that 50 keV is the minimum energy of the lowest energy channel of the ELFIN measurements, but otherwise not particularly significant (see details of ELFIN observations of EMIC-driven precipitation events and their comparison with other scattering mechanisms in Angelopoulos et al., 2023; Artemyev et al., 2023; Grach et al., 2022). Statistics of direct measurements of the energy cutoff of precipitating electrons have shown that EMIC waves often drive sub-relativistic precipitation well below the theoretical minimum resonance energy for the typical frequency of the observed waves. Figures (1a–1f) shows three examples of such sub-MeV electron precipitation driven by EMIC waves and observed by ELFIN. In these events, the spectrum of the precipitating-to-trapped flux ratio shows that EMIC waves are responsible for ≥300 keV precipitation. The absence of <200 keV precipitation bespeaks of the lack of whistler-mode waves as a potential electron scattering mechanism. This is a typical event from ELFIN

observations (see An et al., 2024; Angelopoulos et al., 2023), and consistent with findings from prior studies (Capannolo et al., 2019; Hendry et al., 2017, 2021).

There are four mechanisms that may explain the unexpected sub-relativistic electron precipitations. The two of four are due to changes in either (a) the specific plasma properties or (b) the specific EMIC wave properties. These changes can cause the plasma-to-cyclotron frequency to increase which leads to decreases in the resonance energy (Summers & Thorne, 2003). These can occur either by (a) variations in the equatorial plasma properties relative to expectation from average models, brought about by large-scale convection or low frequency modulations (Zhang et al., 2019), or (b) when the EMIC wave frequency approaches the proton cyclotron frequency (Angelopoulos et al., 2023; Ukhorskiy et al., 2010). While these two mechanisms offer promising perspectives, they do not always work (e.g., Capannolo et al., 2019). The third and fourth mechanisms are more sophisticated: electrons can be scattered below the minimum resonance energy due to (c) nonlinear fractional resonances (Hanzelka et al., 2023, 2024) or (d) due to nonresonant interactions with EMIC wave packets (An et al., 2022; Chen et al., 2016; Grach & Demekhov, 2023), the primary topic of this paper. To be effective, fractional resonances require high wave intensity. The nonresonant interaction model suggests that electrons undergo a net change in their magnetic moment (mostly though a change in their pitch angle) when, due to the finite size of the wave-packet, significant variations in wave amplitude occur over just a few wavelengths. This pitch-angle change accumulates after electrons have encountered several wave packets (or the same wave packet while bouncing back and forth along the field line), allowing for efficient scattering of nonresonant electrons. Shorter wave packets, characterized by the sharpest wave amplitude variations, are more effective. Such electron interactions with finite-size EMIC wave packets extend the effective resonance energy lower, and permit electron scattering even when the electrons are not in resonance with the EMIC wave at its mean wave frequency under an infinite wave packet approximation (An et al., 2022; Grach & Demekhov, 2023; Hanzelka et al., 2023). That the nonresonant interaction mechanism can explain sub-relativistic precipitation in specific events has been demonstrated using case studies with ELFIN data (An et al., 2022, 2024). However, this mechanism has not yet been incorporated into the radiation belt models.

Let us briefly expand upon two of these four mechanisms (second and fourth) for explaining low-energy electron precipitation by EMIC waves (An et al., 2022, 2024; Angelopoulos et al., 2023). The second mechanism relies on cyclotron resonance between low energy electrons (below the typical resonance energy of ∼1 MeV) and the higher frequency but lower intensity tail in the power spectrum of H-band EMIC waves, extending above the peak power frequency in case studies or statistical observations (Angelopoulos et al., 2023). This high frequency tail was statistically determined by Zhang et al. (2016) after performing fast fourier transforms (FFTs) of Van Allen Probes time-series waveform data, under the assumption that the frequency distribution inside the wave packets is a realistic representation of the observed time-series. It was further assumed that high frequency waves (with high $f/f_{cp} \sim 0.6 - 0.9$) from Zhang et al. (2016) follow the usual EMIC wave dispersion relation (close to the cold plasma dispersion relation, see Summers & Thorne, 2003) and, therefore, correspond to high wave numbers providing pitch-angle diffusion for low energy electrons (Angelopoulos et al., 2023). The first of these two assumptions is supported by a recent statistical study (Shi et al., 2024), which found that wave periods at the edge of H-band EMIC wave packets often become much shorter than near the packet center (and peak power), confirming the existence of a finite high frequency wave power tail. In addition, Shi et al. (2024) demonstrated the presence of a finite population of wave packets with peak power at similarly high frequencies, confirming the existence of such high frequency EMIC waves (see also Teng et al., 2019; Asamura et al., 2021, for statistical results of high-frequency EMIC waves) satisfying the usual dispersion relation, validating the second assumption. Many H-band EMIC wave packets likely result from superposition of waves of different frequencies, amplitudes, and phases (Shi et al., 2024), as is the case for whistler-mode chorus packets (Tao et al., 2013; Zhang et al., 2020).

In the fourth mechanism to explain subrelativistic precipitation, nonresonant interactions, the scattering is provided by interactions with wave numbers significantly higher than the wave numbers of the peak-power frequency, highest amplitude waves composing H-band EMIC wave packets, implying that this interaction is indeed nonresonant with the peak-power frequency waves (An et al., 2022, 2024), although it is still resonant with the lower amplitude, higher wavenumber (higher frequency) waves (An et al., 2024; Shi et al., 2024; Xu & Egedal, 2022). This second approach assumes that the observed short duration EMIC wave packets correspond to spatially short wave packets, and further assumes that an FFT in space of these short spatial packets provides the actual distribution of wavenumbers inside such packets (An et al., 2022, 2024). As for the first approach, this

assumption is supported by observations of short wave periods at the edge of packets (Shi et al., 2024), suggesting the presence of real waves with both high frequencies and high wavenumbers.

Accordingly, these second and fourth mechanisms are in fact approximately equivalent, since they both assume a monotonic relationship between wave frequency and wavenumber, and since they both rely on the existence of high wavenumber waves, of high frequencies, at the edge of H-band EMIC wave packets, consistent with observations (Shi et al., 2024). The main difference is that in the second mechanism (Angelopoulos et al., 2023) wavenumbers are inferred from measured wave frequencies using the EMIC wave dispersion relation, whereas the fourth mechanism (An et al., 2022, 2024) is more flexible and can easily accommodate variations away from the usual dispersion relation. In the following, we shall focus on the fourth mechanism of nonresonant interaction with EMIC wave packets for deriving electron pitch-angle diffusion rates, but one should bear in mind that similar results could have been obtained using the second mechanism.

Although there exists a well-developed theoretical approach for calculating the scattering rate of nonresonant interactions (An et al., 2022, 2024; Grach & Demekhov, 2023), merging this approach with the classical quasi-linear treatment of electron diffusion rates can result in a unified methodology over the broadest range of resonance energies—a significant benefit. The main challenge lies in the fact that all existing empirical models of EMIC waves, which are used for evaluating quasi-linear diffusion rates, only incorporate very basic wave spectral characteristics, such as the wave frequency at peak power and an estimate of the average spectral width around this peak, with an assumed Gaussian spectral shape (e.g., see Meredith et al., 2014; Ross et al., 2021). Such empirical models of EMIC waves lack information about wave-packet characteristics, such as the wave packet size which is an essential parameter for the nonresonant model. We aim to use recently collected and analyzed statistics of EMIC wave packets from the Van Allen probes (Shi et al., 2024) to construct a universal approach for generalizing existing diffusion rate models, without requiring any reevaluation of EMIC wave statistics or any significant modification to quasi-linear diffusion codes. In Section 2, we present the main equation describing the nonresonant effect and the main statistical characteristics of EMIC wave packets. In Section 3, we use the Green's function approach to merge the nonresonant formalism with the quasi-linear treatment and provide a simple approximate model for generalized diffusion rates, the $\mathcal{G}$ model. Figures 1g and 1h shows the main result of this merging: the precipitating-to-trapped flux ratio derived from the theoretical model of resonant and nonresonant interactions (RN model, in black) covers a wider energy range and provides a more gradual $j_{\parallel}/j_{\perp}$ decrease with decreasing energy, in comparison with the resonant-only model (R model, in red). Figure 1i confirms that observational $j_{\parallel}/j_{\perp}$ spectra show a similar gradual $j_{\parallel}/j_{\perp}$ decay to lower energies. We plotted observational $j_{\parallel}/j_{\perp}$ spectra together with the R-model spectrum showing low-energy cut-off and $\mathcal{G}$ model spectra (evaluated for two typical values of plasma frequency to gyrofrequency ratios). The $\mathcal{G}$ model, including nonresonant effects, is a statistical model—that is, not fitted to or specifically designed for this event, faithfully overlaps the gray domain of the low-energy part of observational $j_{\parallel}/j_{\perp}$ spectra. The main goal of this paper is to provide this approximate analytical $\mathcal{G}$ model, based on the Green's function approach, that allows the incorporation of nonresonant effects into radiation belt models. Blue curves in Figures 1g and 1h show that this approximation fits the RN model results for nonresonant interactions quite well. We explain details of this approximation in Section 3, and then discuss it in Section 4.

2. Electron Diffusion Model

The general diffusion rate for both nonresonant and resonant interactions has been derived in An et al. (2022), An et al. (2024) and Grach and Demekhov (2023):

$$
\begin{aligned}
D_{\alpha\alpha} &= \frac{e^2 B_w^2 G}{2(\gamma^2-1)\, m^2 c^4 \cos^2\alpha_{eq}\, \tau_b}, \\
G &= \left| \int_{z_l}^{z_u} g(z') e^{i\phi_R(z')} dz' \right|^2, \\
\phi_R &= \int_{z_l}^{z_u} dz' \left(k(z') - \frac{\omega(z')/c}{\sqrt{\gamma^2 - 1 - 2\omega_{ce}(z')\, I_0/(m_{ec}^2)}} \right)
\end{aligned}
\tag{1}
$$

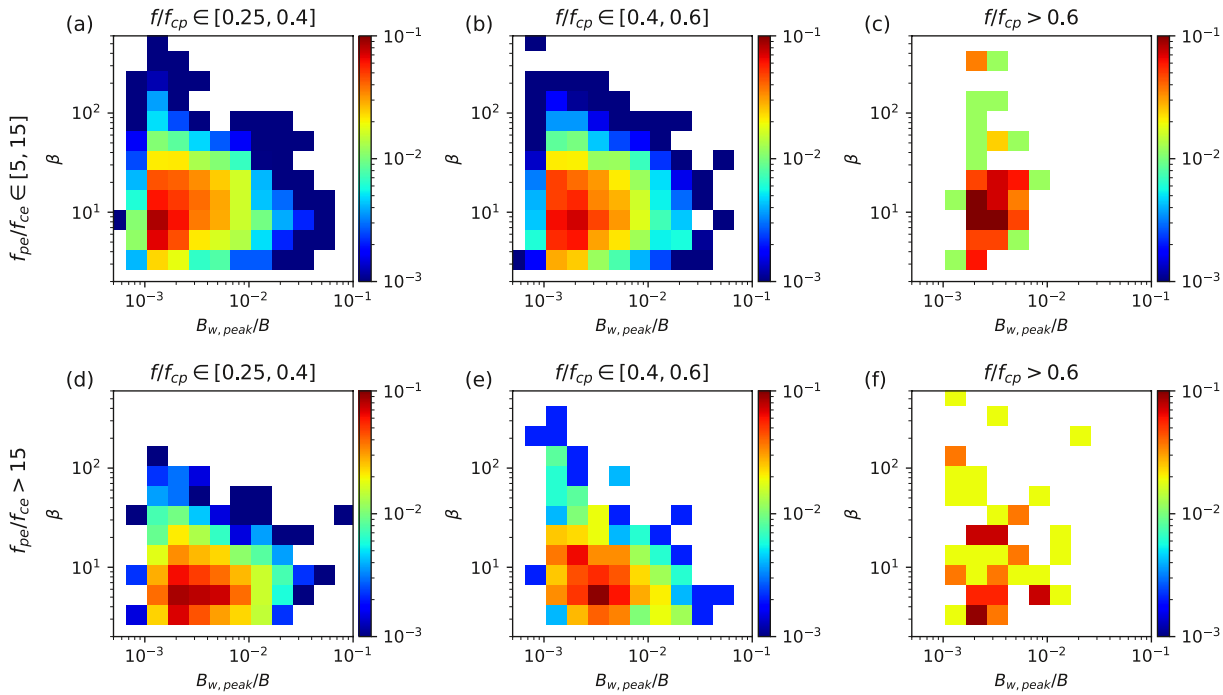

Figure 2. Probability distributions $\mathcal{P}$ of electromagnetic ion cyclotron wave-packet size (β) and normalized wave amplitude ($B_{w,\mathrm{peak}}/B$) at different wave frequency ranges and $f_{\mathrm{pe}}/f_{\mathrm{ce}}$ ranges.

where z is the direction along the magnetic file line, $g(z)$ is the shape function describing the envelope of the wave packet with lower and upper boundaries located at z_l and z_u, respectively (we assume the wave packet center is located at the equator, and the lower and upper bounds are chosen as five times of standard deviations of the Gaussian-shaped wave packet away from the center where the amplitudes are close to zero), B_w is the peak wave amplitude of the wave packet, α_{eq} is the electron equatorial pitch angle, τ_b is the electron bounce period, ϕ_R is the phase integral (I_0 is the zeroth-order magnetic moment, ω_{ce} is the electron cyclotron frequency, and k is the wave number), and γ is the relativistic factor. When the wave is infinitely long with $g(z) = 1$ (i.e., a plane wave), the diffusion rate in Equation 1 includes only resonant interactions and is identical to the classical quasi-linear diffusion rate (Summers & Thorne, 2003; Summers et al., 2007a).

The two main characteristics of the wave field incorporated into Equation 1 are the wave packet shape function and the wave amplitude. To calculate the averaged diffusion coefficient over different wave amplitudes and wave packet size, we collect a statistical distribution of these characteristics using 3 yrs of Van Allen Probe measurements of EMIC waves (Zhang et al., 2016). This data set includes the packet size, frequencies, and amplitude of H-band EMIC waves (see details of methods and wave-packet data set in Shi et al., 2024). Figure 2 shows the joint probability distribution $\mathcal{P}$ of EMIC wave-packets as a function of packet size (β, the number of wave periods inside a wave packet) and normalized wave amplitude ($B_{w,\mathrm{peak}}/B$), derived for three different wave frequency ranges and two different $f_{\mathrm{pe}}/f_{\mathrm{ce}}$ (plasma to electron cyclotron frequency ratio) ranges. The MLT range here is [5, 10] (where most EMIC waves are generated by ion injections and dayside compressional ion heating, see Jun et al., 2021; Jun et al., 2024); results for other MLT sectors ([10, 15] and [15, 20]) can be found in the Supporting Information S1. Note that we do not consider the midnight MLT sector because of poor statistics of EMIC waves. Most waves are observed at frequencies around $[0.25, 0.6]f_{\mathrm{cp}}$, where f_{cp} is the proton cyclotron frequency. The highest probability is around $\beta \sim 10$ and $B_{w,\mathrm{peak}}/B \sim 3 \times 10^{-3}$. Wave packets are generally shorter for higher $f_{\mathrm{pe}}/f_{\mathrm{ce}}$, which may be related to mechanisms of such short wave-packet generation (Shoji & Omura, 2013).

To incorporate the wave statistics into the diffusion coefficient evaluation, we choose a Gaussian for the shape function $g(z) = \exp\left(-0.5z^2/L_z^2\right)$, where $kL_z = \beta$, that is, the observed temporal scale of wave-packet, β (number of wave periods within wave-packets), is transferred to the spatial scale L_z (number of wavelengths within wave-packets) with the wavenumber, k, corresponding to the mean wave frequency. Then we evaluate the diffusion rate

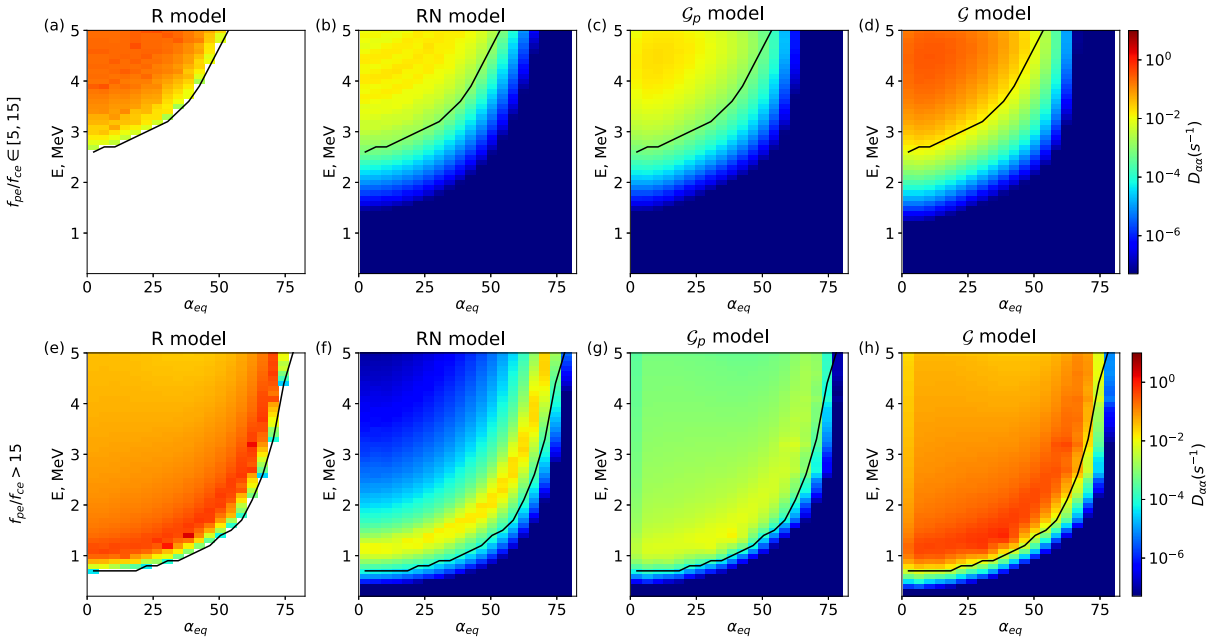

Figure 3. The diffusion rates are depicted for: resonant interactions only (panels a, e), both resonant and nonresonant interactions (panels b, f), Green's function fitting results (panels c, g) obtained with the application of Equations 2 and 3, and rescaled fitting results (panels d, h). Panels (a–d) are for $f_{pe}/f_{ce} \in [5, 15]$, while panels (e–h) are for $f_{pe}/f_{ce} > 15$.

for each bin in (β, $B_{w,\text{peak}}/B$, f/f_{cp}) space (f_{pe}/f_{ce} is retained as an independent variable) and average the diffusion rates over the three dimensions $\langle D_{\alpha\alpha} \rangle = \int D_{\alpha\alpha} \mathcal{P}(\beta, B_w, f)\, d\beta dB_w df$. Figures 3a and 3e show the averaged diffusion rates for only resonant interactions under the assumption of plane waves ($g(z) = 1$) with $f_{pe}/f_{ce} \in [5, 15]$ and $f_{pe}/f_{ce} > 15$, respectively (corresponding to different β distributions). Figures 3b and 3f show the averaged diffusion rates including both resonant and nonresonant interactions with the observation-based distribution of finite wave-packet sizes. The black lines show the minimum resonance energy E_{min}. With the nonresonant effect, electrons below the minimum resonance energy can still be effectively scattered (panels (b, f)): the diffusion rate for the energy above the minimum resonance energy decreases rapidly as energy increases, but remains significant within 0.5 MeV above E_{min}. Note that we assume that wave packets are distributed around the equator and their amplitude decreases exponentially away from it. However, when $g(z) = 1$, there is no amplitude variation, resulting in a higher diffusion rate when resonance occurs at a higher magnetic latitude. This explains the smaller diffusion rates for the $g(z)$ function at high energies of electrons resonating with off-equatorial EMIC waves. In a more sophisticated scheme, there should be some distribution of wave-packet centers, $g(z - z_0)$, permitting direct comparison of $g = 1$ and $g = g(z)$ results. However, in the simplified scheme considered here, we focus on the inclusion of nonresonant effects associated with electron dynamics near the equator which are unaffected by the difference in average wave intensities between $g(z)$ and $g = 1$.

The comparison between panels (a, e) and (b, f) demonstrates the importance of including nonresonant effects in models for energetic (sub-relativistic) electron loss by EMIC waves. Although RN-model diffusion rates (including both resonant and nonresonant interactions) can be evaluated from given wave and plasma parameters, such evaluation requires the modification of existing radiation belt codes with incorporating Equation 1 instead of the classical quasi-linear equations. Moreover, such evaluation requires wave packet sizes, which are not always available in some EMIC wave data sets. To simplify the implementation of RN-model we would like to construct a simple analytical approximation of nonresonant effects, which can be incorporated into all existing diffusion models. In the next section, we use the Green's function approach ($\mathcal{G}$-model) and present the convolution procedure for the resonant diffusion rate that will extend the energy and pitch-angle range of electron scattering using the probability distributions of wave-packet sizes from Figure 2.

Table 1
Fitting Parameters for Green's Function

f_{pe}/f_{ce}	MLT	a_1	a_2	a_3
[5, 15]	(5, 10)	0.5	20	45°
	(10, 15)	0.4	20	
	(15, 20)	0.35	20	
>15	(5, 10)	0.2	6	70°
	(10, 15)	0.25	3	
	(15, 20)	0.2	5	

3. Green's Function Approach

Within this study, the basic idea of the Green's function (convolution) approach is to derive (using a fitting procedure) an analytical function $\mathcal{G}$, that will transform the resonant diffusion rate, $D_R(E, \alpha)$, into a diffusion rate that includes nonresonant effects. To this end, we first introduce $\mathcal{G}_p$ is an intermediate step for fitting:

$$D(E,\alpha) = A(\alpha)\int_0^{\pi/2}\int_{E_{\min}}^{E_{\max}} \mathcal{G}_p\left(E,E',\alpha,\alpha'\right) D_R\left(E',\alpha'\right) dE'\,d\alpha', \quad (2)$$

where $A(\alpha)$ is the magnitude of $\mathcal{G}_p$. This α-dependent amplitude is needed to describe the abrupt decay of the diffusion rate at large pitch-angles. We also introduce $\mathcal{G} = S \cdot \mathcal{G}_p$ with the constant rescaling factor S which ensures alignment of the maximum values (in the entire energy and pitch angle space) between the resonant diffusion rates and the diffusion rates obtained from the convolution procedure. This factor is necessary to align the amplitudes of diffusion rates derived considering wave-packet effects with those derived in previous studies under the assumption of infinite wave-packets.

Inspection of the diffusion rates shown in Figure 3 reveals that $\mathcal{G}_p$ should mainly extend the energy range of scattering for low pitch angles and the pitch-angle range of scattering for high energies. We propose the three-parameter (a_1, a_2 and a_3) function $\mathcal{G}_p$ given by:

$$\mathcal{G}_p\left(E,E',\alpha,\alpha'\right) = \exp\left(-\left(\frac{\alpha-\alpha'}{a_1\sqrt{\sin\alpha'}}\right)^2 - \left(\frac{E-E'}{a_2\sqrt{\cos\alpha'}}\right)^2\right) \quad (3)$$

where a_1 and a_2 depend on MLT and f_{pe}/f_{ce} (as well as $A(\alpha)$ function that should decrease $\mathcal{G}_p$ for high α). The function $A(\alpha) = 0.01\exp(-\alpha/30° - 1/100)$ when $\alpha < a_3$ and $A(\alpha) = 0.01\exp\left(-\alpha/30° - (\alpha/10a_3)^2\right)$ when $\alpha > a_3$. Coefficients of these functions and a_1, a_2, a_3 coefficients are found using two-dimensional least squares fit of the model and directly calculated diffusion rates with nonresonant effects (see Table 1). The fitting parameters for other MLT sectors and f_{pe}/f_{ce} range are also listed in Table 1 and the fitting results are shown in the Supporting Information S1.

Figures 3c and 3g show diffusion rates obtained with the application of Equations 2 and 3 to the resonant diffusion rates from panels (a) and (e). Application of the Green's function ($\mathcal{G}_p$) effectively extends the pitch-angle and energy ranges of electron scattering to match the diffusion rates expected from nonresonant scattering. This is evident when comparing panels (c, g) with panels (b, f) below the black curve (the minimum resonance energy). Such convolution, however, smooths the resonant diffusion rate, and after applying the factor S, the fitting results from function $\mathcal{G}$ are shown in panels (d) and (h), with the same maximum values between the resonant diffusion rates and the diffusion rates obtained from $\mathcal{G}_p$. The comparison between panels (d, h) and panels (a, e) underscores that the diffusion rates calculated using $\mathcal{G}$ model from panels (c, g) closely match the resonant diffusion rates above the minimum resonance energy (within the resonant pitch-angle, energy domain). These results complete the generalization of the diffusion rates related to EMIC waves.

Figures 1g and 1h further demonstrates the potential of the proposed approach for describing low-altitude observations of sub-relativistic electron precipitation. We use the diffusion rates from Figure 3 to calculate the precipitating-to-trapped flux ratio, $j_\parallel/j_\perp$. This calculation was performed with the approximate equation $j_\parallel/j_\perp = 0.9/z_0$ (an approximation valid for $j_\parallel/j_\perp \in [0.11, 1]$, see Angelopoulos et al., 2023), where $z_0 = 2\alpha_{LC}/\sqrt{D_{\alpha\alpha}\tau_b}$ with α_{LC} the electron pitch angle (Li et al., 2013). The values of $j_\parallel/j_\perp$ obtained for three types of diffusion rates are shown in Figures 1g and 1h: we use diffusion rates calculated based only on resonance with the main waves (red curves), diffusion rates with nonresonant effects (i.e., including resonance with waves of much lower amplitude and higher wave number k than the main waves in each packet) included (black curves), and diffusion rates using the Green's function approach (blue curves). Black and blue curves, which both include nonresonant effects, have an extended tail at lower energies and explain the precipitation down to sub-relativistic energies. Figure 1i

demonstrates that the modeled flux ratio $j_{\parallel}/j_{\perp}$ captures the extended low-amplitude tail at lower energies, but the decay of the flux ratio with decreasing energy is more rapid in the model than in observations.

This discrepancy is likely due to the approximations made in the model. In the model, averaging is performed over a wave-packet ensemble, and all packets are assumed to exhibit a smooth Gaussian spatial shape, such that the wave number distribution corresponds to this Gaussian shape (An et al., 2022, 2024). Here, this wave-packet ensemble includes long packets (refer to Figure 2) that, in this simplified model, correspond to smaller wave numbers than shorter packets. In reality, wave packets often do not have a Gaussian shape (for instance, intense long packets may have sharp edges) and they often exhibit significant variations in wave period around their edges (Shi et al., 2024), two effects not yet taken into account in the simplified model but which can lead to a larger fraction of waves at higher wave numbers and, therefore, can cause electron diffusion down to lower energy. Such peculiarities of the wave-packet statistics can be accounted for modeling of a specific event, but should not be important in long-term (storm period) simulations.

4. Conclusions

In this study we used a new theoretical model of nonresonant electron scattering by EMIC waves (An et al., 2022, 2024; Grach & Demekhov, 2023) and a Van Allen Probes database of EMIC wave-packet characteristics (Shi et al., 2024; Zhang et al., 2016) to verify the effects of nonresonant interactions for realistic wave characteristics. Such nonresonant interactions can extend the energy and pitch-angle ranges of electron scattering, and thus should be helpful in the explanation of sub-relativistic electron precipitation events attributed to electron scattering by EMIC waves (see Figure 1 and An et al., 2022; Angelopoulos et al., 2023; Capannolo et al., 2019; Hendry et al., 2017; Hendry et al., 2019). To incorporate nonresonant effects into the existing resonant diffusion rates, we utilized the Green's function approach provided by Equations 2 and 3. These equations represent a useful tool for quantifying the impact of nonresonant interactions on electron diffusion rates, facilitating computations of generalized (including both resonant and nonresonant interactions) electron diffusion rates for studying inner magnetosphere dynamics. The main advantage of this approach is that it does not require a reevaluation of existing diffusion rate models and empirical models of EMIC wave activity (or event-oriented EMIC wave measurements), but instead provides a simple recipe for the generalization of existing resonant diffusion rates. This approach resolves a long-standing problem of sub-relativistic electron precipitation by EMIC waves (Capannolo et al., 2019; Hendry et al., 2017, 2019). A future incorporation of the proposed Green's function approach and of the generalized diffusion rates into radiation belt models could help to verify the usefulness of this approach for long-term electron losses (e.g., Drozdov et al., 2017; Ma et al., 2015). Future application of the method to multi-case studies of EMIC-driven precipitation observed by ELFIN (e.g., Angelopoulos et al., 2023; Capannolo et al., 2023) could provide insights into how efficiently this approach can describe the precipitation spectrum (the ratio $j_{\parallel}/j_{\perp}$) as a function of system parameters (MLT and f_{pe}/f_{ce}).

Data Availability Statement

Waves measured by Van Allen probe are available in https://cdaweb.gsfc.nasa.gov/. Data analysis was done using SPEDAS V4.1 (Angelopoulos et al., 2019). The software can be downloaded from http://spedas.org/wiki/.

Acknowledgments
A.V.A and X.-J. Z. acknowledge support from the NASA Grant 80NSSC23K0108, 80NSSC23K0403, 80NSSC24K0558. X.-J. Z. acknowledges support from the NSF Grant 2329897. V.A. acknowledges support from NSF grants AGS-1242918, AGS-2019950 and NASA contract NAS5-02099. X.A. acknowledges support from the NSF Grant 2108582 and NASA Grant 80NSSC20K0917. We are grateful to NASA's CubeSat Launch Initiative for ELFIN's successful launch in the desired orbits. We acknowledge the early support of the ELFIN project by the AFOSR, under its University Nanosat Program, UNP-8 project, contract FA9453-12-D-0285, and by the California Space Grant program. We acknowledge the critical contributions of numerous volunteer ELFIN team student members.

References

An, X., Artemyev, A., Angelopoulos, V., Zhang, X., Mourenas, D., & Bortnik, J. (2022). Nonresonant scattering of relativistic electrons by electromagnetic ion cyclotron waves in Earth's radiation belts. *Physical Review Letters*, *129*(13), 135101. https://doi.org/10.1103/PhysRevLett.129.135101

An, X., Artemyev, A., Angelopoulos, V., Zhang, X.-J., Mourenas, D., Bortnik, J., & Shi, X. (2024). Nonresonant scattering of energetic electrons by electromagnetic ion cyclotron waves: Spacecraft observations and theoretical framework. *Journal of Geophysical Research: Space Physics*, *129*(3), e2023JA031863. https://doi.org/10.1029/2023JA031863

Angelopoulos, V., Cruce, P., Drozdov, A., Grimes, E. W., Hatzigeorgiu, N., King, D. A., et al. (2019). The Space Physics Environment Data Analysis System (SPEDAS). *Space Science Reviews*, *215*(1), 9. https://doi.org/10.1007/s11214-018-0576-4

Angelopoulos, V., Tsai, E., Bingley, L., Shaffer, C., Turner, D. L., Runov, A., et al. (2020). The ELFIN mission. *Space Science Reviews*, *216*(5), 103. https://doi.org/10.1007/s11214-020-00721-7

Angelopoulos, V., Zhang, X. J., Artemyev, A. V., Mourenas, D., Tsai, E., Wilkins, C., et al. (2023). Energetic electron precipitation driven by electromagnetic ion cyclotron waves from ELFIN's low altitude perspective. *Space Science Reviews*, *219*(5), 37. https://doi.org/10.1007/s11214-023-00984-w

Artemyev, A. V., Angelopoulos, V., Zhang, X. J., Chen, L., & Runov, A. (2023). Dispersed relativistic electron precipitation patterns between the ion and electron isotropy boundaries. *Journal of Geophysical Research (Space Physics)*, *128*(12), e2023JA032200. https://doi.org/10.1029/2023JA032200

Artemyev, A. V., Angelopoulos, V., Zhang, X. J., Runov, A., Petrukovich, A., Nakamura, R., et al. (2022). Thinning of the Magnetotail current sheet inferred from low-altitude observations of energetic electrons. *Journal of Geophysical Research (Space Physics)*, *127*(10), e2022JA030705. https://doi.org/10.1029/2022JA030705

Asamura, K., Shoji, M., Miyoshi, Y., Kasahara, Y., Kasaba, Y., Kumamoto, A., et al. (2021). Cross-energy couplings from Magnetosonic waves to electromagnetic ion cyclotron waves through cold ion heating inside the plasmasphere. *Physical Review Letters*, *127*(24), 245101. https://doi.org/10.1103/PhysRevLett.127.245101

Capannolo, L., Li, W., Ma, Q., Chen, L., Shen, X. C., Spence, H. E., et al. (2019). Direct observation of subrelativistic electron precipitation potentially driven by EMIC waves. *Geophysical Research Letters*, *46*(22), 12711–12721. https://doi.org/10.1029/2019GL084202

Capannolo, L., Li, W., Ma, Q., Qin, M., Shen, X. C., Angelopoulos, V., et al. (2023). Electron precipitation observed by ELFIN using proton precipitation as a proxy for Electromagnetic Ion Cyclotron (EMIC) waves. *Geophysical Research Letters*, *50*(21), e2023GL103519. https://doi.org/10.1029/2023GL103519

Chen, L., Thorne, R. M., Bortnik, J., & Zhang, X.-J. (2016). Nonresonant interactions of electromagnetic ion cyclotron waves with relativistic electrons. *Journal of Geophysical Research*, *121*(10), 9913–9925. https://doi.org/10.1002/2016JA022813

Drozdov, A. Y., Shprits, Y. Y., Usanova, M. E., Aseev, N. A., Kellerman, A. C., & Zhu, H. (2017). EMIC wave parameterization in the long-term VERB code simulation. *Journal of Geophysical Research*, *122*(8), 8488–8501. https://doi.org/10.1002/2017JA024389

Grach, V. S., Artemyev, A. V., Demekhov, A. G., Zhang, X.-J., Bortnik, J., Angelopoulos, V., et al. (2022). Relativistic electron precipitation by EMIC waves: Importance of nonlinear resonant effects. *Geophysical Research Letters*, *49*(17), e99994. https://doi.org/10.1029/2022GL099994

Grach, V. S., & Demekhov, A. G. (2023). Interaction of relativistic electrons with packets of the electromagnetic ion cyclotron waves of finite length and low amplitude. *Plasma Physics Reports*, *49*(7), 901–911. https://doi.org/10.1134/S1063780X23600561

Hanzelka, M., Li, W., & Ma, Q. (2023). Parametric analysis of pitch angle scattering and losses of relativistic electrons by oblique EMIC waves. *Frontiers in Astronomy and Space Sciences*, *10*, 1163515. https://doi.org/10.3389/fspas.2023.1163515

Hanzelka, M., Li, W., Qin, M., Capannolo, L., Shen, X., Ma, Q., et al. (2024). Sub-MeV electron precipitation driven by EMIC Waves through nonlinear fractional resonances. *Geophysical Research Letters*, *51*(8), e2023GL107355. https://doi.org/10.1029/2023GL107355

Hendry, A. T., Rodger, C. J., & Clilverd, M. A. (2017). Evidence of sub-MeV EMIC-driven electron precipitation. *Geophysical Research Letters*, *44*(3), 1210–1218. https://doi.org/10.1002/2016GL071807

Hendry, A. T., Rodger, C. J., Clilverd, M. A., & Morley, S. K. (2021). Evidence of sub MeV EMIC driven trapped electron flux dropouts from GPS observations. *Geophysical Research Letters*, *48*(9), e92664. https://doi.org/10.1029/2021GL092664

Hendry, A. T., Santolik, O., Kletzing, C. A., Rodger, C. J., Shiokawa, K., & Baishev, D. (2019). Multi-instrument observation of nonlinear EMIC-driven electron precipitation at sub-MeV energies. *Geophysical Research Letters*, *46*(13), 7248–7257. https://doi.org/10.1029/2019GL082401

Jun, C.-W., Miyoshi, Y., Kurita, S., Yue, C., Bortnik, J., Lyons, L., et al. (2021). The characteristics of EMIC waves in the magnetosphere based on the Van Allen Probes and Arase observations. *Journal of Geophysical Research (Space Physics)*, *126*(6), e29001. https://doi.org/10.1029/2020JA029001

Jun, C. W., Miyoshi, Y., Nakamura, S., Shoji, M., Hori, T., Bortnik, J., et al. (2024). A triggering process for nonlinear EMIC waves driven by the compression of the dayside magnetosphere. *Geophysical Research Letters*, *51*(1), e2023GL106860. https://doi.org/10.1029/2023GL106860

Jun, C. W., Yue, C., Bortnik, J., Lyons, L. R., Nishimura, Y., & Kletzing, C. (2019). EMIC wave properties associated with and without injections in the inner magnetosphere. *Journal of Geophysical Research (Space Physics)*, *124*(3), 2029–2045. https://doi.org/10.1029/2018JA026279

Kersten, T., Horne, R. B., Glauert, S. A., Meredith, N. P., Fraser, B. J., & Grew, R. S. (2014). Electron losses from the radiation belts caused by EMIC waves. *Journal of Geophysical Research*, *119*(11), 8820–8837. https://doi.org/10.1002/2014JA020366

Li, W., Ni, B., Thorne, R. M., Bortnik, J., Green, J. C., Kletzing, C. A., et al. (2013). Constructing the global distribution of chorus wave intensity using measurements of electrons by the POES satellites and waves by the Van Allen Probes. *Geophysical Research Letters*, *40*(17), 4526–4532. https://doi.org/10.1002/grl.50920

Ma, Q., Li, W., Thorne, R. M., Bortnik, J., Reeves, G. D., Kletzing, C. A., et al. (2016). Characteristic energy range of electron scattering due to plasmaspheric hiss. *Journal of Geophysical Research*, *121*(12), 11. https://doi.org/10.1002/2016JA023311

Ma, Q., Li, W., Thorne, R. M., Ni, B., Kletzing, C. A., Kurth, W. S., et al. (2015). Modeling inward diffusion and slow decay of energetic electrons in the Earth's outer radiation belt. *Geophysical Research Letters*, *42*(4), 987–995. https://doi.org/10.1002/2014GL062977

Meredith, N. P., Horne, R. B., Kersten, T., Fraser, B. J., & Grew, R. S. (2014). Global morphology and spectral properties of EMIC waves derived from CRRES observations. *Journal of Geophysical Research*, *119*(7), 5328–5342. https://doi.org/10.1002/2014JA020064

Millan, R. M., & Thorne, R. M. (2007). Review of radiation belt relativistic electron losses. *Journal of Atmospheric and Solar-Terrestrial Physics*, *69*(3), 362–377. https://doi.org/10.1016/j.jastp.2006.06.019

Mourenas, D., Ma, Q., Artemyev, A. V., & Li, W. (2017). Scaling laws for the inner structure of the radiation belts. *Geophysical Research Letters*, *44*(7), 3009–3018. https://doi.org/10.1002/2017GL072987

Ni, B., Cao, X., Zou, Z., Zhou, C., Gu, X., Bortnik, J., et al. (2015). Resonant scattering of outer zone relativistic electrons by multiband EMIC waves and resultant electron loss time scales. *Journal of Geophysical Research*, *120*(9), 7357–7373. https://doi.org/10.1002/2015JA021466

O'Brien, T. P., & Moldwin, M. B. (2003). Empirical Plasmapause models from magnetic indices. *Geophysical Research Letters*, *30*(4), 1152. https://doi.org/10.1029/2002GL016007

Ross, J. P. J., Glauert, S. A., Horne, R. B., Watt, C. E. J., & Meredith, N. P. (2021). On the variability of EMIC waves and the consequences for the relativistic electron radiation belt population. *Journal of Geophysical Research (Space Physics)*, *126*(12), e29754. https://doi.org/10.1029/2021JA029754

Shi, X., Artemyev, A., Zhang, X.-J., Mourenas, D., An, X., & Angelopoulos, V. (2024). Properties of intense H-band electromagnetic ion cyclotron waves: Implications for quasi-linear, Nonlinear, and Nonresonant wave-particle interactions. *Journal of Geophysical Research (Space Physics)*, *129*(1), e2023JA032179. https://doi.org/10.1029/2023JA032179

Shoji, M., & Omura, Y. (2013). Triggering process of electromagnetic ion cyclotron rising tone emissions in the inner magnetosphere. *Journal of Geophysical Research (Space Physics)*, *118*(9), 5553–5561. https://doi.org/10.1002/jgra.50523

Shprits, Y. Y., Subbotin, D. A., Meredith, N. P., & Elkington, S. R. (2008). Review of modeling of losses and sources of relativistic electrons in the outer radiation belt II: Local acceleration and loss. *Journal of Atmospheric and Solar-Terrestrial Physics*, *70*(14), 1694–1713. https://doi.org/10.1016/j.jastp.2008.06.014

Summers, D., Ni, B., & Meredith, N. P. (2007a). Timescales for radiation belt electron acceleration and loss due to resonant wave-particle interactions: 1. Theory. *Journal of Geophysical Research*, *112*(A4), 4206. https://doi.org/10.1029/2006JA011801

Summers, D., Ni, B., & Meredith, N. P. (2007b). Timescales for radiation belt electron acceleration and loss due to resonant wave-particle interactions: 2. Evaluation for VLF chorus, ELF hiss, and electromagnetic ion cyclotron waves. *Journal of Geophysical Research*, *112*(A4), 4207. https://doi.org/10.1029/2006JA011993

Summers, D., & Thorne, R. M. (2003). Relativistic electron pitch-angle scattering by electromagnetic ion cyclotron waves during geomagnetic storms. *Journal of Geophysical Research*, *108*(A4), 1143. https://doi.org/10.1029/2002JA009489

Tao, X., Bortnik, J., Albert, J. M., Thorne, R. M., & Li, W. (2013). The importance of amplitude modulation in nonlinear interactions between electrons and large amplitude whistler waves. *Journal of Atmospheric and Solar-Terrestrial Physics*, *99*, 67–72. https://doi.org/10.1016/j.jastp.2012.05.012

Teng, S., Tao, X., & Li, W. (2019). Typical characteristics of whistler mode waves categorized by their spectral properties using Van Allen Probes observations. *Geophysical Research Letters*, *46*(7), 3607–3614. https://doi.org/10.1029/2019GL082161

Ukhorskiy, A. Y., Shprits, Y. Y., Anderson, B. J., Takahashi, K., & Thorne, R. M. (2010). Rapid scattering of radiation belt electrons by storm-time EMIC waves. *Geophysical Research Letters*, *37*(9), L09101. https://doi.org/10.1029/2010GL042906

Usanova, M. E. (2021). Energy exchange between Electromagnetic Ion Cyclotron (EMIC) waves and thermal plasma: From theory to observations. *Frontiers in Astronomy and Space Sciences*, *8*, 150. https://doi.org/10.3389/fspas.2021.744344

Usanova, M. E., Mann, I. R., Bortnik, J., Shao, L., & Angelopoulos, V. (2012). THEMIS observations of electromagnetic ion cyclotron wave occurrence: Dependence on AE, SYMH, and solar wind dynamic pressure. *Journal of Geophysical Research*, *117*(A10), 10218. https://doi.org/10.1029/2012JA018049

Wilkins, C., Angelopoulos, V., Runov, A., Artemyev, A., Zhang, X. J., Liu, J., & Tsai, E. (2023). Statistical characteristics of the electron isotropy boundary. *Journal of Geophysical Research (Space Physics)*, *128*(10), e2023JA031774. https://doi.org/10.1029/2023JA031774

Xu, Y., & Egedal, J. (2022). Pitch angle scattering of fast particles by low frequency magnetic fluctuations. *Physics of Plasmas*, *29*(1), 010701. https://doi.org/10.1063/5.0077787

Yahnin, A. G., Yahnina, T. A., Raita, T., & Manninen, J. (2017). Ground pulsation magnetometer observations conjugated with relativistic electron precipitation. *Journal of Geophysical Research (Space Physics)*, *122*(9), 9169–9182. https://doi.org/10.1002/2017JA024249

Yahnin, A. G., Yahnina, T. A., Semenova, N. V., Gvozdevsky, B. B., & Pashin, A. B. (2016). Relativistic electron precipitation as seen by NOAA POES. *Journal of Geophysical Research (Space Physics)*, *121*(9), 8286–8299. https://doi.org/10.1002/2016JA022765

Zhang, X.-J., Li, W., Thorne, R. M., Angelopoulos, V., Bortnik, J., Kletzing, C. A., et al. (2016). Statistical distribution of EMIC wave spectra: Observations from Van Allen Probes. *Geophysical Research Letters*, *43*(24), 12. https://doi.org/10.1002/2016GL071158

Zhang, X. J., Mourenas, D., Artemyev, A. V., Angelopoulos, V., Kurth, W. S., Kletzing, C. A., & Hospodarsky, G. B. (2020). Rapid frequency variations within intense chorus wave packets. *Geophysical Research Letters*, *47*(15), e88853. https://doi.org/10.1029/2020GL088853

Zhang, X.-J., Mourenas, D., Artemyev, A. V., Angelopoulos, V., & Sauvaud, J.-A. (2019). Precipitation of MeV and sub-MeV electrons due to combined effects of EMIC and ULF waves. *Journal of Geophysical Research: Space Physics*, *124*(10), 7923–7935. https://doi.org/10.1029/2019JA026566